Continental-scale multiobservation calibration and assessment of Colorado State University Unified Land Model by application of Moderate Resolution Imaging Spectroradiometer (MODIS) surface albedo

Toshihisa Matsui,[1,2] Adriana Beltrán-Przekurat,[3] Roger A. Pielke Sr.,[3] Dev Niyogi,[4] and Michael B. Coughenour[5]

Received 17 May 2006; revised 5 October 2006; accepted 2 January 2007; published 12 June 2007.

[1] This study attempts to establish the first continental-scale multiobservation calibration and assessment of a land surface model (LSM) over the conterminous United States by using the Colorado State University Unified Land Model (CSU ULM) within the NASA GSFC's Land Information System and the Parameter Estimation (PEST) model. This study aims to calibrate the vegetation and soil optical parameters in different landcover classes by comparing model-predicted surface albedo and those derived from the Moderate Resolution Imaging Spectroradiometer (MODIS) (including black- and white-sky albedo for visible and near-infrared band). The sum of squared deviations (Ψ) between model- and MODIS-derived albedo is iteratively reduced via the Gauss-Marquardt-Levenberg (GML) algorithm. The first calibration process (1) reduced Ψ by about 80% for noncalibrated as well as calibrated seasons and years, (2) revealed the functional biases related to diffuse-radiation upscattering parameters in two-stream canopy radiation scheme (which was fixed before the second calibration), and (3) shows that the parameter related to the leaf angle distribution function could not be tuned. The second calibration was implemented from the lessons learned from the first calibration, and results in the more realistic convergence of the parameters. After calibration, the summertime surface energy budget simulated by offline ULM changed significantly over the less vegetated regions; for example, net shortwave radiation and available energy increased by more than 40 W m^{-2} and radiative temperature increased by more than 1.6 K in the postcalibrated experiment.

Citation: Matsui, T., A. Beltrán-Przekurat, R. A. Pielke Sr., D. Niyogi, and M. B. Coughenour (2007), Continental-scale multiobservation calibration and assessment of Colorado State University Unified Land Model by application of Moderate Resolution Imaging Spectroradiometer (MODIS) surface albedo, *J. Geophys. Res.*, *112*, G02028, doi:10.1029/2006JG000229.

1. Introduction

[2] Land surface models (LSM) diagnose terrestrial mass and energy flux and biogeochemical processes, which are critical for applications in numerical weather forecasting and climate diagnostics. In the last several decades, hydrology and climate communities have developed a number of different types of LSMs for their research applications [*Pitman*, 2003]. Many LSMs participated in the Project for Intercomparison of Land-Surface Parameterization Schemes (PILPS) [*Henderson-Sellers et al.*, 2002]. PILPS' Phase 1 and Phase 2 experiments found a significant diversity in the performances of different LSMs [*Pitman et al.*, 1999]. This is because each LSM contain a number of different functional equations that represent soil-vegetation-atmosphere-transfer (SVAT) processes, and each function consists of different tunable parameters that usually cannot be measured directly or extensively in time and space.

[3] The agreement between model output and observations can be improved by modifying tunable parameters. This process is called model calibration. Model calibration can be accomplished manually (i.e., by hand) for the simply structured LSM. However, as the structures of LSMs become more complicated, a manual calibration becomes difficult even for the experienced modeler. This is because parameterizations within LSMs are nonlinear and coupled; for example, a change in the surface albedo results in the modification of turbulent heat flux, radiative temperature,

[1]Department of Atmospheric Science, Colorado State University, Fort Collins, Colorado, USA.
[2]Now at NASA Goddard Space Flight Center, Greenbelt, Maryland, USA.
[3]Department of Atmospheric and Oceanic Sciences, Cooperative Institute for Research in Environmental Sciences, University of Colorado, Boulder, Colorado, USA.
[4]Department of Agronomy and Department of Earth and Atmospheric Sciences, Purdue University, West Lafayette, Indiana, USA.
[5]Natural Resource and Environmental Laboratory, Colorado State University, Fort Collins, Colorado, USA.

Copyright 2007 by the American Geophysical Union.
0148-0227/07/2006JG000229

photosynthesis, and root-zone soil moisture [*Niyogi et al.*, 1999]. Therefore the hydrology community has been developing an automatic calibration framework that tunes a LSM via nonlinear inversion model [*Gupta et al.*, 1999]. The automatic calibration more effectively improves an LSM with a simpler structure than one with a more complex structure [*Wood et al.*, 1998].

[4] The calibration of an LSM generally requires two types of data: (1) meteorological forcing and (2) ground-truth observations of surface flux and state. The meteorological forcing data is the weather input that drives the LSM to calculate the energy and mass exchange (e.g., turbulent energy flux, runoff) and terrestrial state (e.g., biomass, soil moisture, temperature, and albedo), while surface observational data are used to examine the gaps between observations and model output. Most of the LSMs are usually calibrated or tested at a limited number of sites owing to a lack of data sets required for the calibration. Calibrated tunable parameters at the specific site are not the universal answer, however. It is one possible combination of feasible parameters that satisfies the given calibration period and watershed; i.e., a calibration improves the performances of the LSM for a given calibrated timescale and a given calibrated watershed [*Wood et al.*, 1998; *Lee et al.*, 1995].

[5] LSMs create the spatial and temporal heterogeneity of the land surface energy and mass flux by assuming specific values of tunable parameters for each land-use/landcover (LULC) type and the geographical feature (e.g., topography, soil type, or leaf area). Because accurate spatial prediction of surface energy and mass flux is critical for the prediction of summertime deep cumulus convection and climate sensitivity [*Pielke*, 2001], the performance of an LSM should be assessed at every single numerical grid point within the model domain. Limited site calibration leads to uncertainty in the performance of an LSM, when the LSM has been applied to a region that features different combinations of soils, plants, and geology [*Niyogi et al.*, 1999; *Matsui et al.*, 2005].

[6] Accuracy and horizontal coverage of data sets required for the calibration have been improved and extended in the past several years. Continental-scale high-resolution meteorological forcing has been developed by the Land Data Assimilation System (LDAS) project [*Cosgrove et al.*, 2003]. High-quality satellite data sets (LULC, leaf area index, surface temperature, and albedo) have been operationally derived from the Moderate Resolution Imaging Spectroradiometer (MODIS) aboard the Earth Observation Satellite (EOS) Terra and Aqua, which has provided global coverage since March 2000 [*Justice et al.*, 2002]. A network of ground eddy covariance tower measurements provides fluxes of CO_2, sensible and latent heat, and soil moisture, which are not directly available from satellite remote sensing [*Baldocchi et al.*, 2001]. A framework is needed that makes best use of the newly available data sets to calibrate and enhance the performance of LSMs. Otherwise it is becoming very difficult to evaluate an actual improvement of the LSM.

[7] This study attempts to establish the continental-scale multiobservation calibration and assessment of an LSM over the conterminous United States (CONUS). This regional calibration framework uses the Colorado State University Unified Land Model (CSU ULM) within the Land Information System (LIS) [*Peters-Lidard et al.*, 2004] coupled with the Parameter Estimation (PEST) model [*Doherty*, 2004]. The continental-scale calibration process has three objectives. The first objective is to directly improve the performance of an LSM at a continental scale by tuning (or generalizing) the LULC- and geography-dependent parameters by minimizing the model-observation discrepancy for all the grid points within the model domain. The second objective is to determine the extent to which improvement in the performance of the LSM can be achieved by adjusting tunable parameters (obtained from a literature review) versus changing model structure. The third objective is to assess the performance between a limited-site calibration and a new large-scale calibration.

[8] This study consists of a two-part series. This paper describes the calibration methodology and surface albedo calibration. Follow-up study [*Matsui*, 2006] shows calibration of the land surface temperatures and turbulent heat fluxes. Surface albedo and associated net shortwave radiation are critical components of the surface energy and mass flux in an LSM [*Dickinson*, 1983], and the surface net radiation modulate the performance of the SVAT scheme (including surface turbulent flux and land surface temperature). Although the ULM initialization uses a consistent set of the MODIS LAI and LULC data, the ULM does not produce surface spectral albedos that are consistent with the MODIS radiances, because of differences in the sophistication and assumptions of the canopy radiative transfer algorithms and soil albedo configurations. This discrepancy has been reported in a number of previous studies [*Oleson et al.*, 2003; *Zhou et al.*, 2003; *Tian et al.*, 2004; *Wang et al.*, 2004]. Thus surface albedo must be estimated and its representation calibrated before the land-surface temperature calibration takes place.

[9] This paper is organized as follows. Section 2 describes a calibration methodology via the Gauss-Marquardt-Levenberg (GML) algorithm. Section 3 describes the data sets required for the calibration, including a brief description of the CSU ULM (section 3.1), the North American LDAS meteorological forcing (section 3.2), MODIS surface product for the model initialization (section 3.3), and spatially complete snow-free MODIS surface albedo that is used for model calibration (section 3.4). Section 4 describes the parameterizations and tunable parameters (two-stream canopy radiative transfer in section 4.1 and soil albedo in section 4.2), and the calibration domain and periods (section 4.3). Section 5 presents the results of precalibration (section 5.1) and postcalibration (section 5.2), and describes the manual correction of the functional error in the canopy radiative transfer model and second calibration result (section 5.3). The new set of tuned parameters is validated for a noncalibrated period (section 5.4), is compared with those derived from limited-time and limited-site calibration (section 5.5), and is tested for the sensitivity of surface turbulent heat fluxes and skin temperatures (section 5.6). Study results are summarized in section 6.

2. Parameter Estimation (PEST) Model: Gauss-Marquardt-Levenberg Algorithm

[10] Parameter Estimation (PEST) model is a freely distributed optimization software, which uses a robust

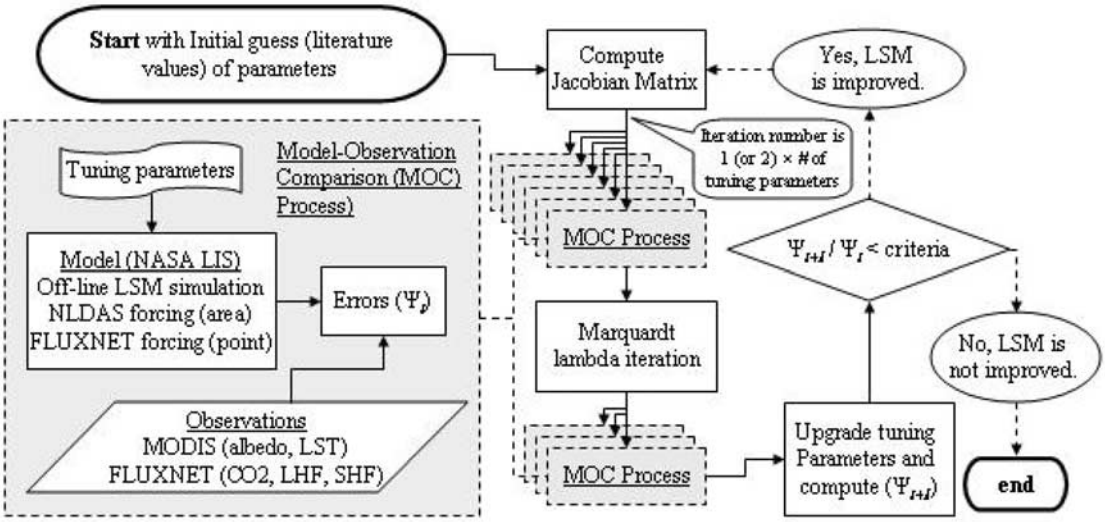

Figure 1. Flow chart of the calibration system. The Part I study uses MODIS data only to compute the objective function Ψ. The Part II study uses MODIS and FLUXNET simultaneously. Model-observation comparison (MOC) processes are distributed in the parallel computing environment.

Gauss-Marquhardt-Levenberg (GML) algorithm. The GML algorithm combines the advantages of the Gauss-Newton method and the steep descent method and therefore provides faster and more efficient convergence toward the minima of an objective function (Ψ: weighted sum of squared deviation between model and observation). The best set of parameter is selected from within reasonable ranges by adjusting the values until the discrepancies between the LSM-generated values and the corresponding observations are reduce to a minimum in the weighted least squares sense [*Doherty*, 2004]. PEST has been used in other nonlinear inversion problems, for example, a surface energy and carbon exchange model [*Wang et al.*, 2001], a distributed watershed model [*Liu et al.*, 2005], and a nutrient transportation model [*Baginska et al.*, 2003].

[11] Figure 1 depicts the calibration process in the PEST. While continental-scale calibration requires significant machine time especially for computing the Jacobian matrix (the partial derivative of error as a function of each parameter), the parallel mode of PEST allows us to use multi-CPUs for ensemble simulations that significantly reduces the required time (by nearly 30 times) [*Doherty*, 2004]. For this study, we used a Mac Xserve G5, consisting of 15 servers with dual 64-bit Mac G5 processors. Thus the maximum operating speed reaches to 135 gigaflops, enabling the completion of the calibration process in several days.

[12] It should be noted that the population-evolution-based global optimization method generally performs better than the pure local search algorithm, because the global optimization method can avoid becoming stuck at multiple local optima in the parameter space [*Duan et al.*, 1993]. A recent development of the global optimization method enables an efficient calibration process [*Vrugt et al.*, 2003]. However, it generally requires a computational cost that is as much as 10 times that of the local search algorithm, and is impractical to apply to the high-resolution continental simulation in this study. Thus we use the GML local searching algorithm, and show that it effectively reduces the apparent biases by generalizing the tunable parameters that satisfy the entire grid in the focused domain. This can be achieved mostly after the initial few iterations of local searching. We also emphasize the importance of evaluating the functional errors based on the postcalibration biases, as well as that this study does not aim to develop an effective calibration method. This study examines the performance of large-scale calibration in comparison with a traditional limited-site calibration.

3. Tools and Data Sets

3.1. LSM: Colorado State University Unified Land Model and Initialization

[13] The Colorado State University (CSU) Unified Land Model, hereafter denoted as ULM, is the numerical land-surface model used in this study. The basic numerical schemes and code are extracted from the Community Land Model (CLM) 2.0 [*Oleson et al.*, 2004], the General Energy and Mass Transfer Model (GEMTM) [*Chen and Coughenour*, 1994], and the Land Ecosystem-Atmosphere Feedback (LEAF) model [*Walko et al.*, 2000]. Detailed soil-vegetation-atmosphere transfer parameterizations are described in the follow-up study [*Matsui*, 2006]. The model includes a 10-layer soil, a two-component (sunlit and shaded) vegetation canopy, and 1 to 13 subgrid tiles. ULM has been developed within the NASA GSFC's Land Information System (LIS) that contains several different LSMs and a wide variety of surface boundary conditions and meteorological forcings. The offline simulations of LSM can be tested anywhere on globe down to the urban-resolving scale [*Peters-Lidard et al.*, 2004].

3.2. Meteorological Forcing: North American Land Data Assimilation System

[14] High-quality atmospheric forcing data sets are critical for an LSM calibration. This study uses the assimilated forcing data sets derived by the multi-institutional North American Land Data Assimilation System (NLDAS) project

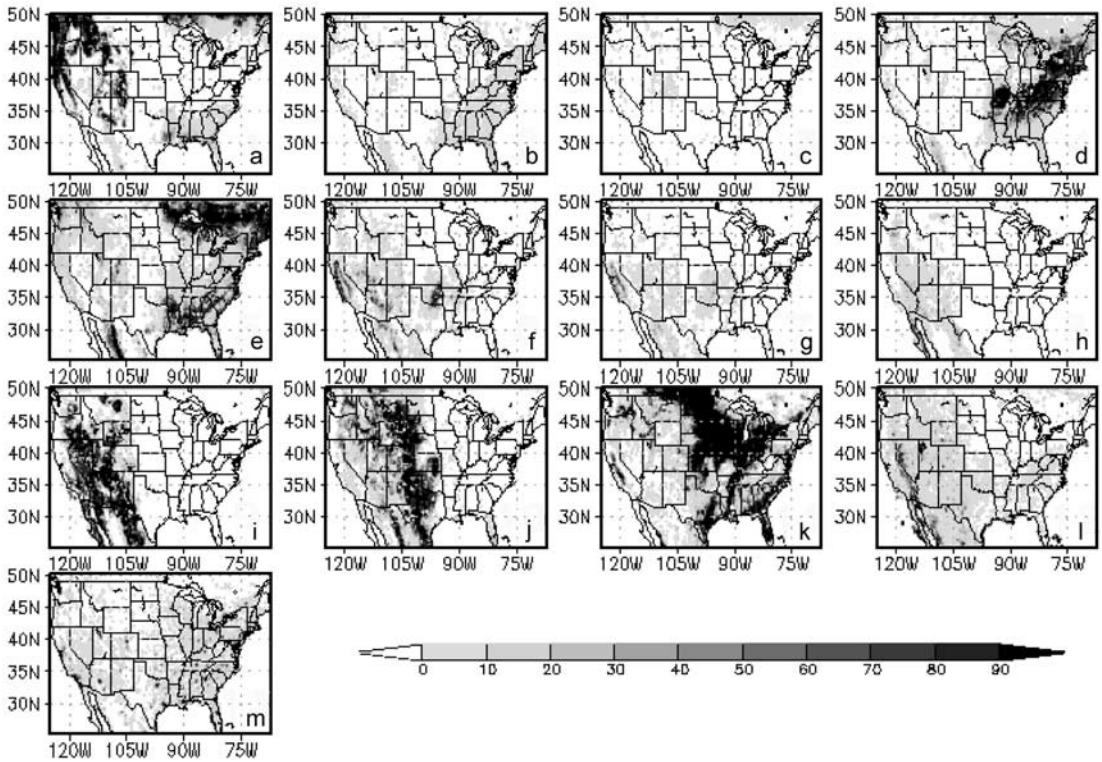

Figure 2. Distribution of fractional coverage of UMD LULC classes: (a) evergreen needleleaf forests, (b) evergreen broadleaf forests, (c) deciduous needleleaf forests, (d) deciduous broadleaf forests, (e) mixed forests, (f) woodlands, (g) wooded grasslands, (h) closed, shrublands, (i) open shrublands, (j) grasslands, (k) croplands, (l), barren, and (m) urban.

[*Cosgrove et al.*, 2003]. Hourly National Weather Service Doppler radar-based (WSR-88D0) precipitation analyses were used to disaggregate the daily National Center for Environmental Prediction (NCEP) Climate Prediction Center (CPC) gauge-based precipitation to produce an hourly observation-based precipitation data set. Surface downwelling solar and thermal radiation is derived from Geostationary Operational Environmental Satellite (GOES) radiation data. Surface air temperatures, water vapor mixing ratios, horizontal winds, and surface pressures are derived from NCEP Eta Data Assimilation System (EDAS) output fields. These comprehensive forcing data sets are archived on a 0.125° grid box at every hour across the conterminous United States (details given by *Cosgrove et al.* [2003]). The NLDAS meteorological field is used to force the CSU ULM on a 1-hour time step.

3.3. Satellite-Based Surface Observation: Initialization for the CSU ULM

[15] A 0.25-degree subgrid LULC map was compiled from the MODIS-based University of Maryland (UMD) 1-km LULC data [*Hansen et al.*, 2000]. The UMD LULC map contains 13 LULC classes. This study arranged the minimum tile fraction of 0.13% in the 0.25° grid in order to fully utilize the 1-km information of the MODIS LULC data. Figure 2 shows the fractional coverage of UMD LULC classes in the study area. Vegetation amount is represented by a combination of green leaf area index (LAI), dead LAI, and stem area index (SAI), all of them derived from monthly composites of the MODIS 1-km LAI from Boston University (hereafter denoted as BU LAI) [*Myneni et al.*, 2002]. The BU LAI product is exceptional in terms of the sophisticated algorithm used and the extensive validation work [*Knyazikhin et al.*, 1998; *Yang et al.*, 2006]. For LAI retrievals, the BU LAI uses a six-biome classification aggregated from the UMD LULC classes. Thus BU LAI can be directly reassigned to the LAI in one of the 13 UMD LULC classes. The 1-km LAI data are aggregated for each UMD LULC classes on the 0.25° grid map for the initialization of the ULM. Dead LAI is derived from the subtraction of green LAI in a previous month to a current month, assuming that dead foliage falls within a month [*Dorman and Sellers* 1989]. SAI is computed as 20% of maximum LAI (L_{max}) of each UMD LULC class, whereas for grasslands SAI is computed from the difference between the L_{max} and green LAI. An L_{max} map was derived from 2000–2005 data sets of monthly BU LAI for each LULC type on each grid. Because ULM uses the one-dimensional canopy radiative transfer model, vegetation fraction is defined as the canopy transmittance computed from the two-stream canopy radiative transfer model (TCRT). This configuration can avoid double counting of the surface reflectance ratio for vegetation fraction and LAI retrievals [*Matsui et al.*, 2005].

3.4. Satellite-Based Surface Observation: MODIS Spectral Albedo

[16] The MODIS instrument aboard the EOS Terra satellite has been providing important information for land surface

properties with local overpass times around 10:30 AM/PM [*Justice et al.*, 2002]. Data quality of the MODIS land product is significantly better than those of the Advanced Very High Resolution Radiometer (AVHRR), because of the sensor on-orbit calibration [*Xiong et al.*, 2003], quality flags, and validation projects [*Morisette et al.*, 2002]. In addition to the MODIS LULC and BU LAI map for ULM's initialization, we use the MODIS spatially complete spectral surface albedo [*Moody et al.*, 2005] in this study and land-surface temperature (LST) [*Wan et al.*, 2002] in follow-up study for calibration and evaluation of the performance of the offline ULM. This study does not utilize other MODIS land products, such as surface evaporation fraction and net primary production, since they are derived from the surface spectral albedo, LAI, LULC and LST data using their own assumed relationships. In other words, the spectral albedo and LST are considered to be the data more directly related to the MODIS-observed radiance.

[17] The spatially complete snow-free MODIS albedo data sets are used to calibrate leaf and soil optical properties in ULM (see section 4). The MODIS albedo was generated through a semi-empirical, kernel-driven linear bidirectional reflectance distribution function (BRDF). This BRDF relies on the 16-day composite of the atmospherically corrected MODIS surface reflectance. The product of MODIS albedo consists of local noon black-sky (for direct radiation) and white-sky (for diffuse radiation) albedo [*Schaaf et al.*, 2002]. A comparison with field measurement from the Surface Radiation Budget Network (SURFRAD) show that the MODIS surface albedo generally meets an absolute accuracy requirement of 0.02, with the root mean square errors less than 0.018 [*Jin et al.*, 2003]. In this study, this uncertainty of MODIS albedo is not taken into account for optimization process, but for the analysis of postcalibrated and precalibrated model albedo biases. Since this study intends to calibrate the vegetation and soil optical parameters, snow-free filled MODIS albedo products are used. The filled albedo product is a value-added product derived from MODIS spectral albedo by filling the missing values (including snow-covered pixels) or low-quality values [*Moody et al.*, 2005]. A temporal interpolation technique imposes pixel-level and local regional ecosystem-dependent phenological behavior onto retrieved pixel temporal data, while regional unique pixel-level information is well maintained. The resulting snow-free spatially complete white- and black-sky surface spectral albedo maps are archived onto 1-min global map [*Moody et al.*, 2005]. For calibration work, 1-min MODIS data were aggregated onto the 0.25°-grid map, if more than 95% of land pixels are available in a 0.25°-grid cell.

[18] This study uses the four different types of albedo: surface black- and white-sky albedo at visible (VIS) and near-infrared (NIR) bands, which corresponds to the direct and diffuse albedo at the VIS and NIR bands computed from the two-stream canopy radiative transfer model (TCRT) [*Dickinson*, 1983; *Sellers*, 1985]. The calibration of both black- and white-sky albedo is necessary for the ULM, because their accuracies are directly linked to the performance of sunlit- and shaded-canopy photosynthesis and net radiation in the ULM (and is described in the follow-up study [*Matsui*, 2006]). The effect of snow on the surface albedo was mechanically removed (snow component in the albedo was set to be zero in the numerical code) in this study, because this study aims to calibrate plant and soil optical properties against the snow-free MODIS surface albedo. Snow albedo will be calibrated in a future study.

[19] The PEST (and GML) algorithms are able to handle an error covariance matrix in an estimation process by incorporating grid-dependent (or value-dependent) weighting functions. However, the error structures in the MODIS surface albedo are only known as a flat value with a 2% uncertainty level [*Jin et al.*, 2003]. Thus the weight is assigned as unity for all the MODIS albedo values in this study.

4. Tunable Parameters and Calibration Periods

4.1. Two-Stream Canopy Radiative Transfer (TCRT)

[20] Surface spectral albedo is parameterized by the two-stream canopy radiative transfer model (TCRT) [*Dickinson*, 1983; *Sellers*, 1985] and empirical soil albedo model [*Idso et al.*, 1975]. Soil albedo is used for the lower boundary condition of TCRT for vegetated tiles, while it represents the surface albedo for nonvegetated tiles (urban and bare-grounds class). Albedos in all subgrid tiles are averaged on the basis of the fraction of subgrid tile coverage ($0 \sim 1$) to represent the total grid albedo.

[21] The TCRT model has been widely used in different LSMs [e.g., *Xue et al.*, 1991; *Dickinson et al.*, 1993; *Sellers et al.*, 1996; *Oleson et al.*, 2004], because of its accuracy and computational efficiency in comparison with multistream or three-dimensional canopy radiative transfer [*Dickinson et al.*, 1987]. The TCRT model also plays an important role in computing the extinction coefficient of within-canopy sunlight penetration that is used for the sunlit and shaded components of canopy, photosynthetic capacity, and actually photosynthesis rates in the ULM.

[22] *Dickinson* [1983] originally proposed to solve the canopy radiative transfer via the two-stream approximation,

$$-\overline{\mu}\frac{dI^{\uparrow}}{dL} + [1 - \omega + \omega\beta]I^{\uparrow} - \omega\beta I^{\downarrow} = \omega\overline{\mu}K(\mu)\beta_o \exp(-K(\mu)L) \tag{1}$$

$$-\overline{\mu}\frac{dI^{\downarrow}}{dL} + [1 - \omega + \omega\beta]I^{\downarrow} - \omega\beta I^{\uparrow} = \omega\overline{\mu}K(\mu)(1 - \beta_o)\exp(-K(\mu)L), \tag{2}$$

where $I^{\uparrow}$ and $I^{\downarrow}$ are the upward and downward diffuse radiative flux normalized by the incident flux; μ is the cosine of the solar zenith angle; $K(\mu)$ is the optical depth of direct beam per unit leaf (or stem) area, and $K(\mu) = G(\mu)/\mu$; $G(\mu)$ is the relative projected area of leaf (or stem) in the direction of $\cos^{-1}\mu$, and $G(\mu) = \phi_1 + \phi_2\mu$ (where $\phi_1 = 0.5 - 0.633\chi_L - 0.33\chi_L^2$ and $\phi_2 = 0.877(1 - 2\phi_1)$); χ_L is departure of leaf angles from a random distribution; $\overline{\mu}$ is the average inverse diffuse optical depth per unit leaf (or stem) area, and $\overline{\mu} = \int_0^1 [\mu'/G(\mu')]d\mu' = \frac{1}{\phi_2}\left[1 - \frac{\phi_1}{\phi_2}\ln\left(\frac{\phi_1 + \phi_2}{\phi_1}\right)\right]$ (where μ' is the direction of scattered flux); ω is the scattering

coefficient, and $\omega = \rho + \tau$; ρ is leaf-stem albedo; τ is the leaf-stem transmittance; L is the cumulative leaf-stem area index; β and β_o are upscattering fraction for diffuse and direct radiation, respectively. The upscattering parameter for diffuse radiation is inferred from the analysis of *Norman and Jarvis* [1975],

$$\omega\beta = 0.5 \cdot \left[\rho + \tau + (\rho + \tau)\left(\frac{1 + \chi_l}{2}\right)^2\right]. \tag{3}$$

The upscattering fraction for direct radiation can be analytically derived from equations (1) and (2) with the assumption of single scattering ($\omega \to 0$) and semi-infinite canopy ($L \to \infty$) [*Dickinson*, 1983],

$$\omega\beta_o = \frac{1 + \overline{\mu}K(\mu)}{\overline{\mu}K(\mu)} a(\mu), \tag{4}$$

where $a(\mu)$ is single scattering albedo

$$a(\mu) = \frac{\omega}{2}\frac{G(\mu)}{\mu\phi_2 + G(\mu)} \cdot \left[1 - \frac{\mu\phi_1}{\mu\phi_2 + G(\mu)} \ln\left(\frac{\mu\phi_1 + \mu\phi_2 + G(\mu)}{\mu\phi_1}\right)\right]. \tag{5}$$

The analytic solution requires the inputs of the scattering coefficients of leaf and stem ($\omega = \rho + \tau$), soil albedo (α_{soi}, see the next section), total LAI and SAI, departure of leaf angles from a random distribution (χ_L), and the angle of the solar radiation (μ) (see the detailed analytic solution in work by *Sellers* [1985] and *Oleson et al.* [2004]).

[23] In this study, tunable parameters include leaf reflectance at the VIS and NIR bands (ρ_{leaf}^{VIS} and ρ_{leaf}^{NIR}, respectively), dead leaf and stem reflectance for the VIS and NIR bands (ρ_{stem}^{VIS} and ρ_{stem}^{NIR}, respectively), and the departure of leaf angles from a random distribution (χ_L). The leaf-stem element reflectance (ρ) are computed from the average of leaf and stem reflectances on the basis of the weight of LAI and SAI. The equations applied to the VIS and NIR leaf and stem transmittance (τ) are kept the same as the ratio between the initial set of leaf reflectance and transmission in order to prevent an unrealistic ratio between leaf reflectance and transmittance due to an overfitting in the calibration process.

4.2. Soil Albedo

[24] Initial model experiment uses the global soil color map, which contains nine classes of soil color type that have values of dry and saturated (50% of dry value) soil albedo [*Reynolds et al.*, 1999]. This global soil map is not tunable, and the footprint size is too large (2.5° × 2.5° grid size) to represent the spatial variability of soil albedo on the grid size used in this study. Thus we introduced a tunable soil albedo map as a function of the log-normalized difference of maximum leaf area index (L_{max}) (see section 3.3) (*LND*).

$$LND = \frac{\ln(L_{\max}) - \ln(0.2)}{\ln(7) - \ln(0.2)}. \tag{6}$$

LND is closely related to the Normalized Difference Vegetation Index (NDVI), because LAI is derived as an exponential function of NDVI [*Myneni et al.*, 2002]. The values 0.2 and 7 are assigned as the minimum and maximum LAI within the domain. The *LND* should have a relationship with the topsoil organic fraction, because the maximum LAI is a good indicator of plant production rate and standardized soil respiration rate [*Reichstein et al.*, 2003]. It is also well known that higher topsoil organic fraction tends to lower the soil albedo [e.g., *Jensen* 2000, Figure 13–8]. Thus an empirical function is introduced to relate *LND* to dry soil VIS and NIR albedo:

$$\alpha_{dry}^{VIS} = \frac{0.01}{a^{VIS} + b^{VIS}LND} \tag{7}$$

$$\alpha_{dry}^{NIR} = \frac{0.01}{a^{NIR} + b^{NIR}LND}, \tag{8}$$

where a^{VIS}, b^{VIS}, a^{NIR}, b^{NIR} are tunable parameters, and "*dry*" and "*sat*" refer to the dry and saturated (defined by the wetness fraction) soil moisture conditions. The proposed equations and tunable parameters can fit any possible pattern of expected relationship between the soil albedo and *LND*. Saturated soil albedo (α_{sat}^{VIS} and α_{sat}^{NIR}) is assumed to be 50% of the dry albedo [*Reynolds et al.*, 1999].

[25] Temporally varying soil albedo is derived from dry and saturated soil albedo, wetness fraction (Δ) in top-soil moisture [$\Delta = \eta/\eta_{\max}$ where η is volumetric soil moisture ($m^3\ m^{-3}$) and $\eta_{\max}$ is porosity ($m^3\ m^{-3}$)], and solar zenith angle [*Idso et al.*, 1975]. For dry soil ($\Delta < 0.3$), soil albedo is a sum of dry soil albedo and a correction factor of solar zenith angle A_ϕ [For direct radiation: $A_\phi = \{\exp[0.003286 \cdot \phi^{1.5}] - 1\}/100$. For diffuse radiation, A_ϕ is integrated for all solar zenith angles for direct radiation (= 0.034).],

$$\alpha_{soi}^{VIS} = \alpha_{dry}^{VIS} + A_\phi \tag{9}$$

$$\alpha_{soi}^{NIR} = \alpha_{dry}^{NIR} + 0.5A_\phi. \tag{10}$$

For wet soil ($\Delta < 0.5$), soil albedo is a sum of saturated soil albedo and a correction factor of solar zenith angle

$$\alpha_{soi}^{VIS} = \alpha_{sat}^{VIS} + A_\phi \tag{11}$$

$$\alpha_{soi}^{NIR} = \alpha_{sat}^{NIR} + 0.5A_\phi. \tag{12}$$

For intermediate soil, ($0.3 < \Delta < 0.5$), soil albedo is linearly interpolated from values between saturated and dry albedo (equations (9)–(12)),

$$\alpha_{soi}^{VIS} = \alpha_{dry}^{VIS} - \frac{(\Delta - 0.3)\left(\alpha_{dry}^{VIS} - \alpha_{sat}^{VIS}\right)}{0.2} \tag{13}$$

$$\alpha_{soi}^{NIR} = \alpha_{dry}^{NIR} - \frac{(\Delta - 0.3)\left(\alpha_{dry}^{NIR} - \alpha_{sat}^{NIR}\right)}{0.2}. \tag{14}$$

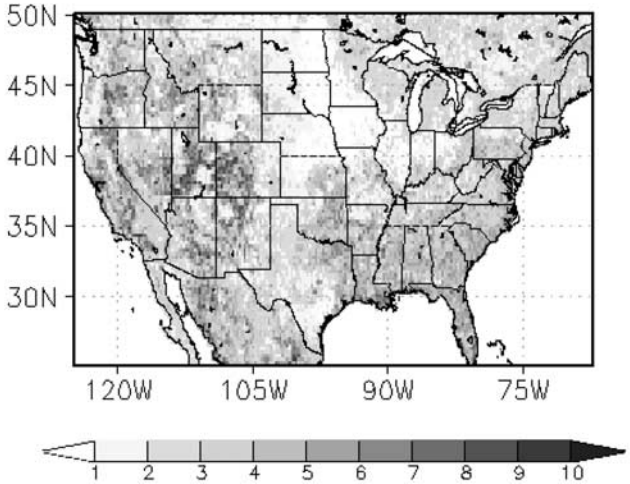

Figure 3. Number of subgrid tiles per modeled grid cell.

4.3. Calibration Domain and Period

[26] The domain size covers approximately the conterminous United States and northern Mexico (latitude of 25°N to 50°N, longitude of 125°W to 65°W) and a grid size of 0.25° × 0.25° (Figure 3). The domain and grid size are configured close to those of NLDAS meteorological forcing. The simulation domain comprises of 16,648 land grid cells and total 61,883 subgrid tiles. The number of subgrid tiles per grid cell is close to one over the croplands in the Midwest, whereas it ranges up to 11 over the southeast and western portion of the domain (Figure 3).

[27] While the MODIS spatially complete surface spectral albedo data set is available from March 2000 to December 2004, we selected 3 months from 2000, March, July and November, for the calibration due to computational time constraints. These 3 months characterize the early development, maturity and senescence, respectively, of the vegetation over United States (Figure 4). The sensitivity of soil albedo (a^{VIS}, b^{VIS}, a^{NIR}, b^{NIR}) to the surface albedo can be relatively large in March, since both LAI and SAI are small over most the regions including the broadleaf and mixed forested areas. The contribution of soil albedo is almost negligible when the sum of LAI and SAI becomes greater than three [*Goudriaan*, 1977]. Thus the contribution of leaf reflectance (ρ_{leaf}^{VIS} and ρ_{leaf}^{NIR}) becomes large in July over the eastern portion of domain and coastal regions in the western United States Because of the senescence of the vegetation in November, the contribution of the stem/dead leaf reflectance (ρ_{stem}^{VIS} and ρ_{stem}^{NIR}) becomes large over the deciduous forests. Over the central United States, owing to small LAI, soil albedo is the key parameter that controls the spectral albedo throughout the seasons. Top-layer (0 ∼ 2 cm) soil moisture has different spatial distributions between March, July, and November so that the parameterized soil albedo could be calibrated as a function of soil moisture. Thus multimonth albedo calibration is designed to balance the calibrating weight of the optical properties between leaf, stem/dead leaf, and soil surface. The total number of calibrating points in the 3-month period is 175,800, including black and white-sky albedo at the VIS and NIR bands. The large number and variations of simulation points enables a more robust calibration process than a limited-site calibration does. Each monthly simulation is separately performed for March, July, and November.

5. Results

5.1. Experiments Before Calibration

[28] Table 1 shows the initial set of tunable parameters for each UMD LULC class. According to the correspondence between UMD LULC and BU LAI vegetation classes, the tunable parameters for surface albedo are the same between evergreen needleleaf and deciduous needleleaf forests, evergreen broadleaf and deciduous broadleaf forests, woodland and wooded grasslands, closed and open shrublands (Table 1). In order to avoid unrealistic convergence, upper and lower bounds are assigned for tunable parameters for forests and savannas classes, respectively: ρ_{leaf}^{VIS} (0.08, 0.2), ρ_{leaf}^{NIR} (0.3, 0.6), ρ_{stem}^{VIS} (0.08, 0.3) and ρ_{stem}^{NIR} (0.25, 0.7). Values for the precalibration tunable parameters correspond to those that are commonly used in the community [*Bonan et al.*, 2002; *Dorman and Sellers*, 1989], and are displayed in Table 1. χ_L of savannas, crops and shrubs are set to be zero (random distribution). The precalibration ULM simulation used the existing global soil color map [*Reynolds et al.*, 1999].

[29] Figure 5a shows the spatial map of differences in local-noon surface spectral albedo between the MODIS observations and the precalibration ULM (i.e., MODIS − ULM). In March and November, ULM overestimates the VIS albedo over the central United States, where LAI is small. These biases are similar between black and white VIS albedo, but appear to be slightly larger in white albedo. Large errors appear at the NIR band. The largest overestimation of ULM exists in the central United States for all the months. In July, ULM underestimates the black NIR albedo across the Appalachian Mountains, Midwest, and the western edge of U.S. ULM overestimates the white NIR albedo over the most of the domain in all the months.

[30] Figure 5b shows descriptive statistics (*m*: mean, *s*: standard deviation, and *rmse*: root-mean-square error) and scatterplots of the errors (MODIS − ULM) in the local-noon albedo (× 100) for the tile fraction (0.8 ∼ 1.0) of each LULC type. Black and white sky VIS albedos show small scatter ($s < 2.0$) and biases ($m < 2.0$) of errors in all forest classes, savannas, and croplands, while large variations and biases are observed in shrublands, grasslands, bare ground, and urban. The ULM overestimates the black and white VIS albedo in shrublands, grasslands and urban. The overestimation of VIS albedo in shrublands and grasslands corresponds to the blue-shaded regions over the central U.S in March and November 2000 (Figure 5a). The ULM also slightly overestimates the white VIS albedo in needleleaf forests, broadleaf forests, and mixed forests, but this is almost within the uncertainty ranges (<2.0) in the operational MODIS albedo product (Jin 2003). Strong variations and biases exist in all the LULC classes for NIR albedo. The ULM tends to underestimate the black NIR albedo in needleleaf forests, broadleaf forests and savannas, which corresponds to the red regions of black NIR albedo in July (Figure 5a). The ULM strongly overestimates ($m < -5.0$) NIR albedos in mixed forests, grasslands, croplands and

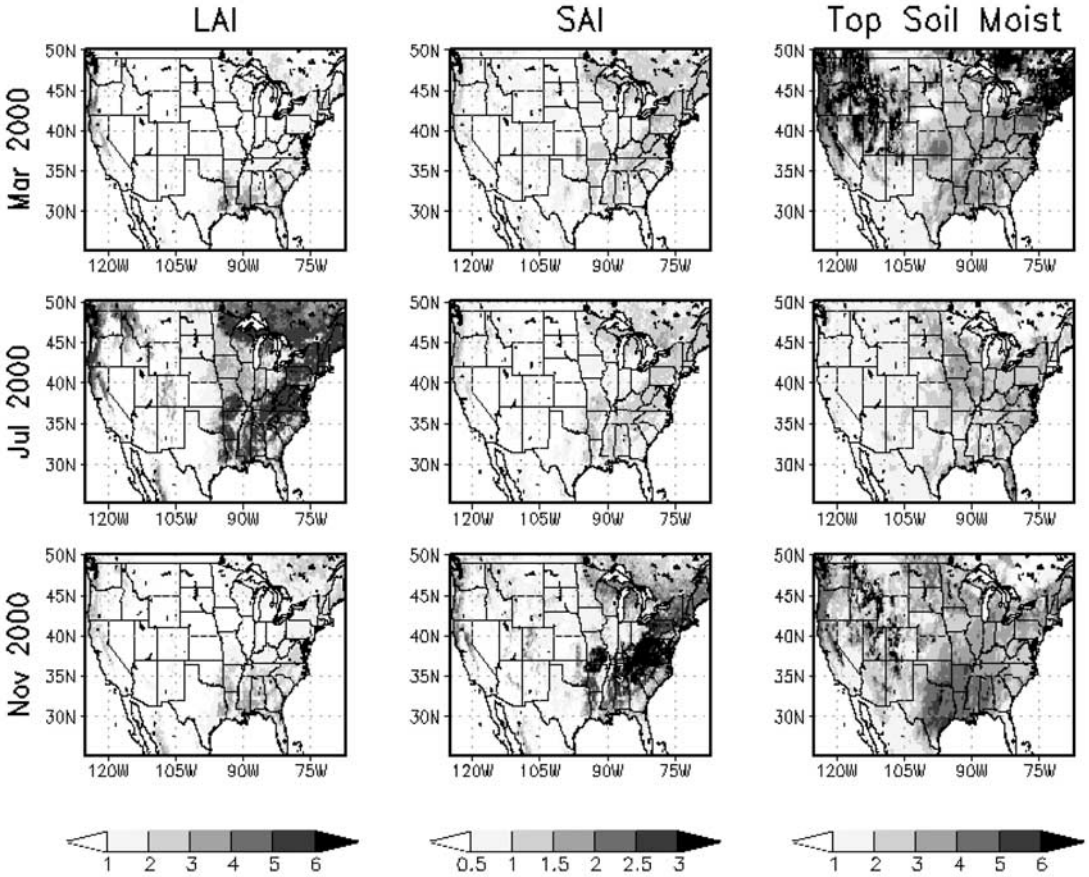

Figure 4. Monthly mean of leaf area index (LAI), dead leaf and stem area index (SAI), top-layer ($0 \sim 2$ cm) soil moisture (kg m^{-2}).

urban classes. Those overestimations characterize the extensive blue area of white NIR albedo in Figure 5a. An interesting pattern of albedo bias in the ULM is that biases in white sky albedo are larger than those in black sky albedo. This is consistent with the finding from *Wang et al.* [2004], and can be explained by the fact that a difference between black- and white-sky albedo in the ULM (i.e., TCRT) is larger than that in the MODIS albedo. This will be further discussed in the following section.

5.2. First Calibration Experiment

[31] The calibration process takes approximately five iterations to achieve the convergence (approximately 300 model runs). Most of the errors were reduced after

Table 1. Tunable Parameters of Each LULC Class Before the Calibration[a]

UMD Class Number and Description	BU LAI	ρ_{leaf}^{VIS}	ρ_{leaf}^{NIR}	ρ_{stem}^{VIS}	ρ_{stem}^{NIR}	χ_L
1. evergreen needleleaf forests	needleleaf forests	0.070	0.350	0.160	0.380	0.00
3. deciduous needleleaf forests						
2. evergreen broadleaf forests	broadleaf forests	0.100	0.450	0.160	0.380	0.250
4. deciduous broadleaf forests						
5. mixed forests	. . .	0.100	0.450	0.160	0.380	0.250
6. woodlands	savannas	0.070	0.350	0.160	0.380	0.00
7. wooded grasslands						
8. closed shrublands	shrubs	0.100	0.450	0.160	0.380	0.00
9. open shrublands						
10. grasslands	grasses/cereal crops	0.110	0.580	0.360	0.580	−0.30
11. croplands	broadleaf crops	0.110	0.580	0.160	0.380	0.00

[a]Precalibration soil albedo uses the global soil albedo map [*Reynolds et al.*, 1999].

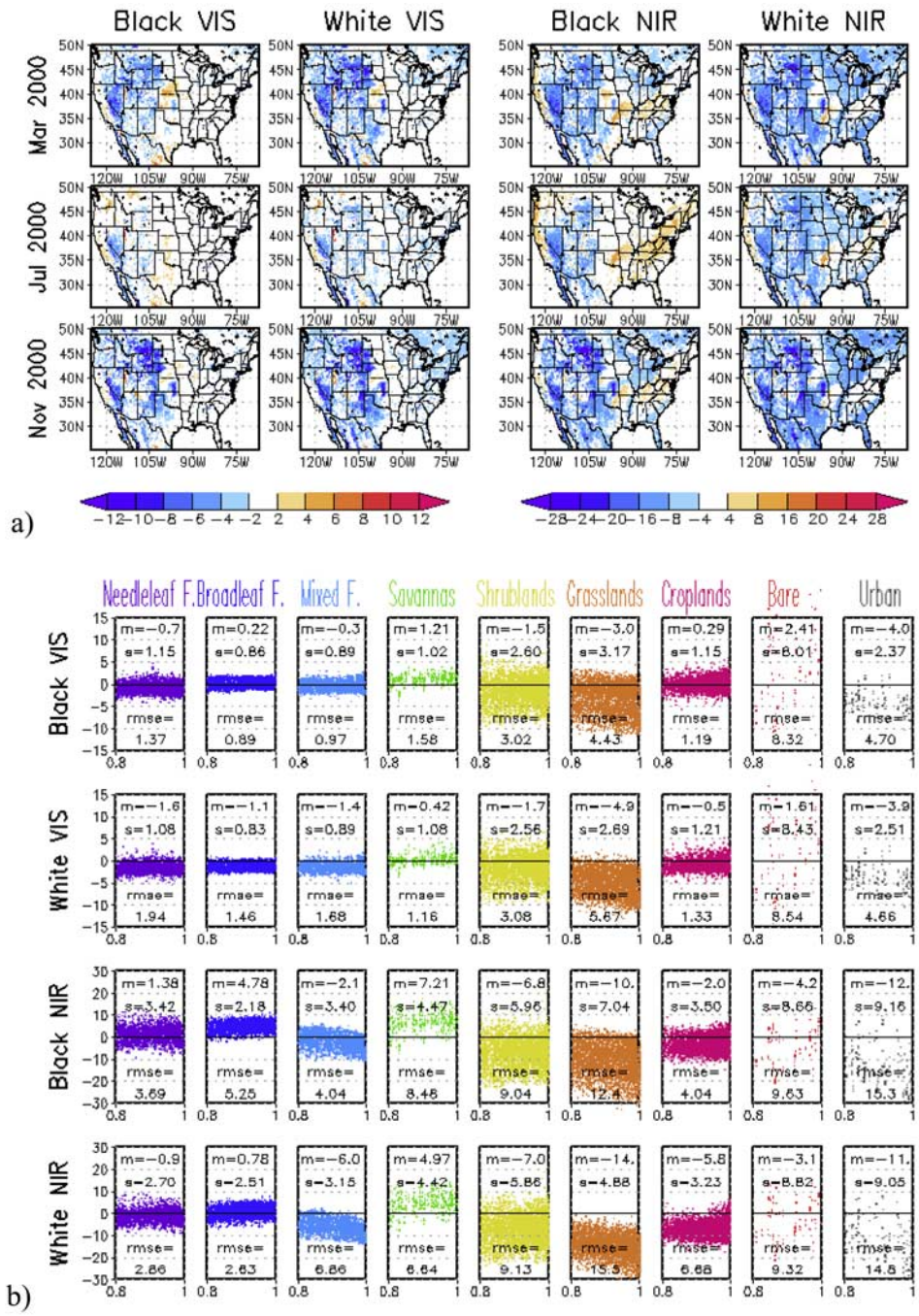

Figure 5. (a) Spatial map of precalibration differences (MODIS − ULM) in spectral surface black and white albedos (× 100). Note that VIS and NIR albedo use different scales. (b) Scatterplots and statistics (*m*, mean; *s*, standard deviation; and *rmse*, root mean square error) of the precalibration difference (MODIS − ULM) in spectral surface black and white albedo (× 100). The x axis represents the fraction (0.8 ∼ 1.0) of each landcover class. VIS and NIR albedo use different scales in the y axis.

the first and second iterations. The entire calibration process results in the final Ψ of 1.12×10^6, which is 18.3% of Ψ in the experiment before the calibration ($\Psi = 6.12 \times 10^6$). Table 2 shows the resultant parameters for each LULC class and soil albedo parameterization. Maximum relative changes of VIS leaf reflectance (ρ_{leaf}^{VIS}) occur in broadleaf and mixed forest. Broadleaf forest increased about 50% of the initial ρ_{leaf}^{VIS} until at the high bound (0.15), while mixed forest decreased about half of the initial ρ_{leaf}^{VIS}. In NIR leaf reflectance the absolute changes are quite large (∼0.14), although the relative changes are small. ρ_{leaf}^{NIR} was decreased in the mixed forests, shrublands, grasslands, and croplands, while it was increased in the needleleaf forests, broadleaf forests, and savannas. VIS stem reflectance (ρ_{stem}^{VIS}) shows a quite variety of changes. All the forest classes decrease the ρ_{stem}^{VIS} near the low bound (0.08). Shrublands increased by

Table 2. Tunable Parameters of Each LULC Class After the Initial Calibration[a]

UMD Class Number and Description	BU LAI	ρ_{leaf}^{VIS}	ρ_{leaf}^{NIR}	ρ_{stem}^{VIS}	ρ_{stem}^{NIR}	χ_L
1. evergreen needleleaf forests	needleleaf forests	0.047	0.376	0.094	0.342	−0.208
3. deciduous needleleaf forests						
2. evergreen broadleaf forests	broadleaf forests	**0.15**	0.516	0.096	0.426	**−0.400**
4. deciduous broadleaf forests						
5. mixed forests	. . .	0.054	0.338	**0.080**	0.292	**0.600**
6. woodlands	savannas	0.074	0.420	0.234	0.551	−0.017
7. wooded grasslands						
8. closed shrublands	shrubs	0.081	0.329	0.327	0.622	−0.240
9. open shrublands						
10. grasslands	grasses/cereal crops	0.132	0.44	0.158	0.364	**0.600**
11. croplands	broadleaf crops	0.095	0.477	0.149	0.321	**0.600**

[a]In boldface are the parameters that reach the upper or lower boundaries. Soil parameters are $a^{VIS} = 0.0524$, $b^{VIS} = 0.070$, $a^{NIR} = 0.0285$, and $b^{NIR} = 0.0263$.

about 50% of the initial ρ_{stem}^{VIS}, while grasslands decreased by half of the initial ρ_{stem}^{VIS}. NIR stem reflectance (ρ_{stem}^{NIR}) substantially increased in the broadleaf forest (~63%), savannas, and shrublands, while it decreased in the grasslands considerably (38.3%). The convergence of the departure of leaf angles from a random distribution (χ_L) appears to be unusual in some classes. Broadleaf forests were expected to range from the random to the horizontally oriented distribution; however, it decreased χ_L to the lower bound (−0.4: vertically oriented leaf). Grasslands were expected to range from the random to the vertically oriented distribution; however, it increased χ_L to the higher bound (0.6: horizontal leaf). The mixed forests and croplands also increased χ_L to the higher bound (0.6: horizontal leaf). This unrealistic χ_L causes a problem in predicting the daytime diurnal cycle of within-canopy sunlight penetration and consequently the sunlit and shaded components of photosynthesis and net radiation. For example, a canopy with completely horizontally oriented leaves has a constant rate of sunlight penetration during daytime. This tends to overestimate the sunlight penetration (sunlit component of canopy) for local morning/evening time, while underestimating the sunlight penetration around local noon.

[32] Figure 6a shows the spatial map of differences (MODIS − ULM) in surface spectral albedo between the postcalibration ULM and the MODIS. The calibration process significantly reduced the biases of ULM albedo over the central United States in the VIS band, and also reduced the biases of NIR albedo in most of the domain. In the VIS band, the underestimations of the ULM albedo (red spots) appear to be in the area near the Great Salt Lake in Utah and barren land in central Mexico.

[33] Figure 6b shows the statistics and scatterplots of biases after calibration for each LULC class. In shrublands and grasslands, the mean values of the errors in VIS albedo range within the uncertainty level of the MODIS product [*Jin et al.*, 2003]. In addition, the spread (standard deviation) of errors in grasslands becomes about 50% smaller than those of the precalibration: 1.41 versus 3.17 for black-sky albedo and 1.46 versus 2.69 for white-sky albedo (Figure 5b). This means that the new adjustable soil albedo parameterization together with tuned vegetation optical parameters improved the spatial representation of surface albedo in the ULM. On the other hand, errors in bare and urban-buildup classes have not been improved in terms of the RMSE, because the total grid number of these classes in the domain is too small to account for in the objective function. In addition, in urban regions, LAI is arbitrarily fixed to zero in the ULM. This might be unrealistic in the urban and suburban regions, where urban buildup and sidewalk trees coexist. Therefore a manual calibration is currently needed for the urban pixels.

[34] In the NIR band, biases (absolute values of mean error) in black-sky and white-sky albedo are decreased after the calibration for all LULC classes. However, black-sky NIR albedo in ULM appears to be slightly underestimated, because the biases of all the classes (excepting urban) of the albedo are positive, while the white NIR albedo in the ULM appears to be less biased. This means that the difference between black and white albedo in the ULM is still slightly larger than that in the MODIS albedo even after the calibration. This bias cannot be fixed by modulating the tunable parameters; it appears to be a functional bias, which will be investigated in the following section.

5.3. Second Calibration Experiment

[35] In order to investigate the functional bias of the TRCT function, we plot the diffuse- and direct-radiation upscattering fraction ($\omega\beta$ and $\omega\beta_o$ defined in equations (3) and (4)) for three different values of χ_L (−0.4, 0.0, and 0.6) as a function of cosine of solar zenith angle in Figure 7a. The diffuse-radiation upscattering fractions are larger than the direct-radiation upscattering parameter for any solar zenith angle. This is not possible, because the diffuse radiation is an integration of all angles of the direct radiation; i.e., diffuse-radiation upscattering fraction should be within the range of the direct-radiation upscattering fraction. We found that this is due to the fact that the

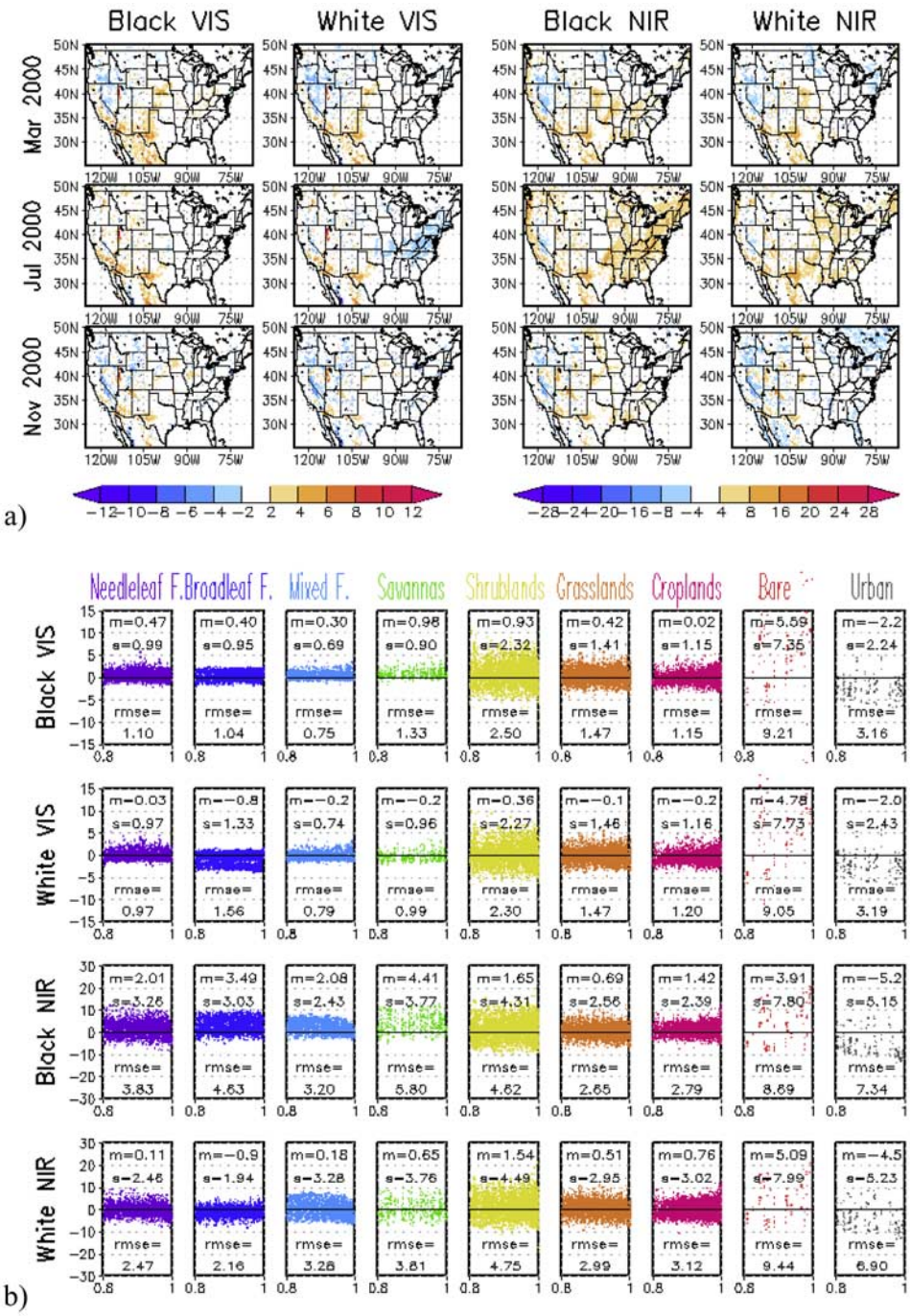

Figure 6. (a) Same as Figure 5a, but after the initial calibration. (b) Same as Figure 5b, but after the initial calibration.

definitions of the upscattering fractions in equation (3) and (4) are taken from different sources. The $\omega\beta$ is acquired from the analysis of *Norman and Jarvis* [1975], while $\omega\beta_o$ is derived from the analytic solution with the assumption of single scattering and semi-infinite canopy [*Dickinson*, 1983].

[36] Thus the definition of upscattering fraction for diffuse radiation is modified so as to be consistent with that for direct radiation. Numerically, we average the direct-radiation upscattering fraction for nine sky angles similar to the canopy model of *Goudriaan* [1977],

$$\omega\beta = \frac{\sum_{i=1}^{9} \frac{1+\overline{\mu}K(\mu_i)}{\overline{\mu}K(\mu_i)} a(\mu_i)}{9}, \quad where \quad \mu_i = \cos[(i-1)\cdot 10 + 5]. \tag{15}$$

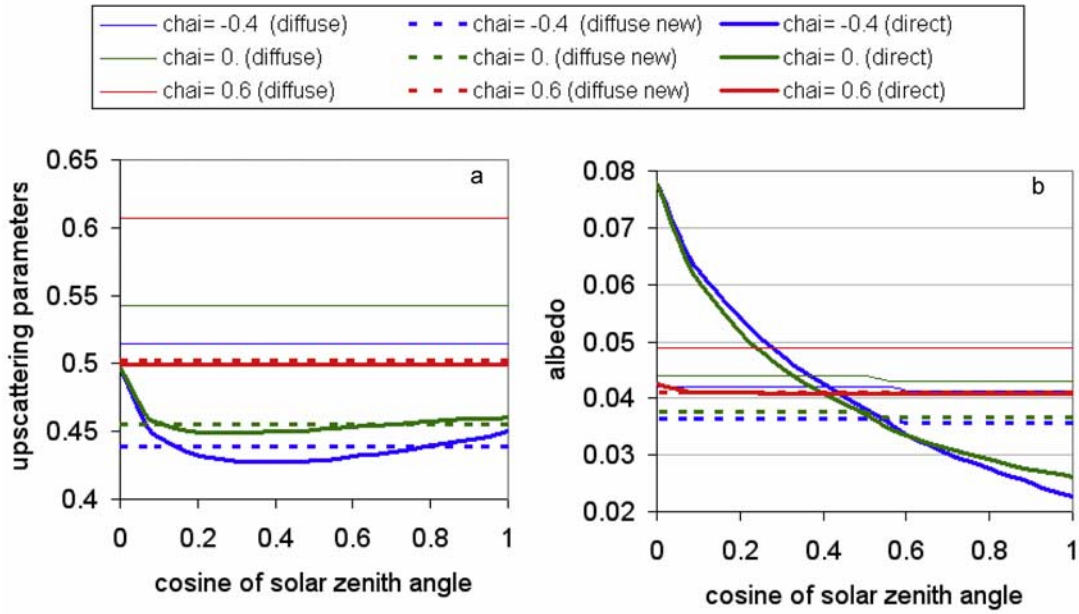

Figure 7. Upscattering fractions and albedo computed from TCRT (LAI = 3, $\rho = 0.1$, $\tau = 0.05$, $\alpha_{soi} = 0.1$). (a) Upscattering fraction for diffuse-radiation (solid thin line), direct radiation (solid thick line), and modified version of diffuse radiation (dashed line). (b) Surface albedo for diffuse radiation (solid thin line), direct radiation (solid thick line), and modified version of diffuse radiation (dashed line).

Figure 7a shows that a new diffuse-radiation upscattering function together with the original value. It is now within the ranges of the direct-radiation upscattering function, and it is physically reasonable. We have computed the albedo for diffuse radiation by using the original formula (equation (3)) and the new formula (equation (15)) (LAI = 3, $\rho = 0.1$, $\tau = 0.05$, $\alpha_{soi} = 0.1$). The new function reduces the white albedo from the original formulae (Figure 7b). For a cosine of solar zenith angle close to the unity, the differences between black and white sky albedos become smaller with the new functions. This new function does not slow down the computational time of the TCRT model for a long-term integration, because the modified diffuse-radiation upscattering fraction (equation (15)) needs to be computed once a day, and it is kept in the computer memory.

[37] A second calibration was implemented from the lessons learned from the first calibration (1) fixed the functional error in diffuse-radiation upscattering fraction, (2) manually fixed the surface albedo for the urban class (0.06 (VIS) and 0.20 (NIR) based on the mean albedo of the urban pixels from the MODIS, and (3) fixed χ_L as the initial value (not calibrated) to prevent the unrealistic diurnal cycle of within-canopy sunlight penetration. The calibration process is completed with these conditions, and it takes approximately the same number of time steps to reach the final Ψ of 1.24×10^6, which is comparable to that of the initial calibration (1.12×10^6), and 20.2% of Ψ in the experiment before the calibration ($\Psi = 6.12 \times 10^6$).

[38] Table 3 shows the final set of the tuned parameters. VIS leaf and stem reflectance (ρ_{leaf}^{VIS} and ρ_{stem}^{VIS}) do not diverge

Table 3. Tunable Parameters of Each LULC Class After the Second Calibration[a]

UMD Class Number and Description	BU LAI	ρ_{leaf}^{VIS}	ρ_{leaf}^{NIR}	ρ_{stem}^{VIS}	ρ_{stem}^{NIR}	χ_L
1. evergreen needleleaf forests	needleleaf forests	0.061	0.418	0.135	0.357	**0.00**
3. deciduous needleleaf forests						
2. evergreen broadleaf forests	broadleaf forests	0.113	0.517	0.150	0.457	**0.250**
4. deciduous broadleaf forests						
5. mixed forests	. . .	0.070	0.388	0.131	0.386	**0.250**
6. woodlands	savannas	0.088	0.494	0.217	0.588	**0.00**
7. wooded grasslands						
8. closed shrublands	shrubs	0.107	0.355	0.182	0.667	**0.00**
9. open shrublands						
10. grasslands	grasses/cereal crops	0.124	0.539	0.193	0.380	**−0.30**
11. croplands	broadleaf crops	0.116	0.566	0.156	0.320	**0.00**

[a]In boldface are the parameters that are invariant during the calibration. Soil parameters are $a^{VIS} = 0.0543$, $b^{VIS} = 0.0529$, $a^{NIR} = 0.0279$, and $b^{NIR} = 0.0236$.

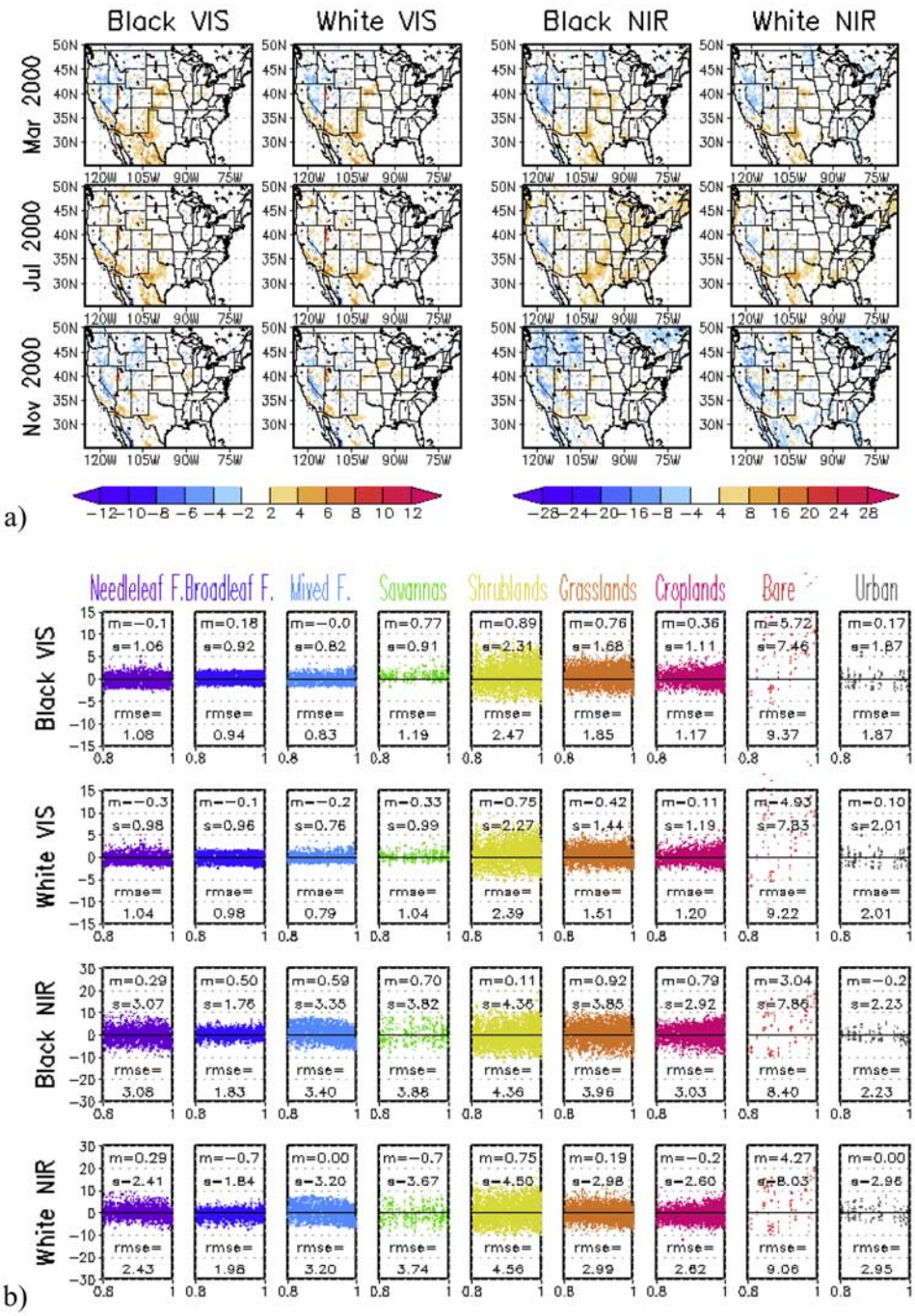

Figure 8. (a) Same as Figure 5a, but after the manual correction and second calibration. (b) Same as Figure 5b, but the manual correction and second calibration.

from the initial value in comparison with the first calibration results in Table 2. NIR leaf and stem reflectance (ρ_{leaf}^{NIR} and ρ_{stem}^{NIR}) are changed notably from the initial set of values in Table 1. The highest NIR leaf reflectance is cropland (0.566), and the lowest is shrubland (0.355). The highest NIR stem reflectance is shrubland (0.667), while the lowest is cropland (0.320). It seams that values between the stem and leaf reflectance in shrubland and cropland compensated each other during the calibration process.

[39] Figure 8a shows the spatial map of differences (MODIS − ULM) in surface spectral albedo between the second calibrated ULM and MODIS. Similar to the map after the initial calibration, the additional calibration process and manual correction of the function in the TCRT model considerably reduced the biases of ULM albedo. Again, in the VIS band, the underestimation of the ULM albedo (red spots) appears in the same places as before.

[40] Figure 8b shows the statistics and scatterplots of biases for each LULC class. VIS black- and white-sky albedo in the three forest classes virtually have no biases, and two standard deviations are mostly within the uncertainty ranges (<2.) of the operational MODIS albedo

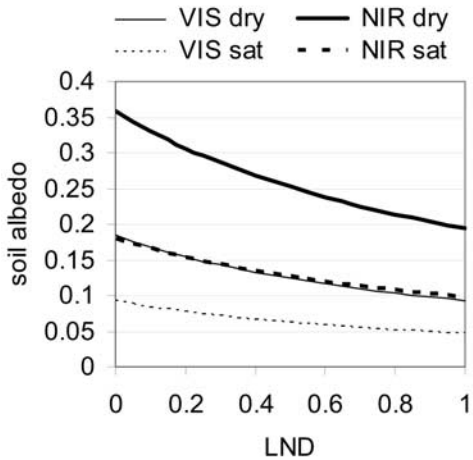

Figure 9. Dry and saturated soil albedo as a function of *LND* (see definition in section 4.2) with a set of tuned parameters (a^{VIS} = 0.0543, b^{VIS} = 0.0529, a^{NIR} = 0.0279, b^{NIR} = 0.0236).

product [*Jin et al.*, 2003]. Characteristics of biases of VIS black- and white albedo for the other LULC classes are quite similar to those in the first calibration experiments. Although standard deviations are slightly high, the mean biases of the NIR black- and white-sky albedo are also improved (<2.) from the precalibration and the first calibration experiments, except for bare ground. By manually fixing the albedo, the biases and standard deviation of all types of albedo, including the urban class, are improved in comparison with the precalibration and first calibration experiments.

[41] Finally, Figure 9 shows the fitted soil albedo values as a function of *LND* with a set of tuned parameters (a^{VIS} = 0.0543, b^{VIS} = 0.0529, a^{NIR} = 0.0279, b^{NIR} = 0.0236). Both VIS and NIR albedos gradually decrease as *LND* decreases. The calibrated soil VIS albedo ranges from 0.18 to 0.09, whereas the Reynolds' soil color map ranges from 0.24 to 0.10. The calibrated soil NIR albedo ranges from 0.36 to 0.19, whereas the Reynolds' soil color map ranges from 0.48 to 0.20. For both VIS and NIR band, the lowest values of albedo are very similar between the calibrated soil albedo and Reynolds' map. Soil VIS albedo is 50% of the NIR albedo, which is exactly the same ratio that Reynolds' soil albedo map specifies. Overall, the tunable albedo ranges are within realistic values compared to Reynolds' map, while minimizing the difference between the simulated and observed albedo.

5.4. Validation of Calibrated Albedo in Different Years and Seasons

[42] This section validates the tuned surface albedo in the ULM for March, July, and November of 2001 to 2004, using precalibrated and postcalibrated optical parameters (Table 1 and Table 3). The precalibrated and postcalibrated albedos are compared in terms of the objective function (Ψ) - the sum of squared errors between model and observations.

[43] Figure 10a shows the objective functions for black- and white-sky VIS and NIR albedo. Precalibration has far greater values of total objective function in all years than those of the postcalibrated experiments. The largest component of the errors is attributed to the white-sky NIR albedo in the precalibration experiments [cf. *Wang et al.*, 2004]. It is clear that the manual correction of the functional error and the calibration process significantly reduced the objective function not only in the calibrated year (2000) but also in the noncalibrated years (2001 $\sim$ 2004). For all years, Ψ of the postcalibration experiments are approximately 20% of that of precalibration experiment.

[44] In addition, ULM was applied in the three seasons between the calibrated months in 2000: April–May–June (AMJ), August–September–October (ASO), and December–January–February (DJF), with precalibration and postcalibration parameters (Table 1 and Table 3). Figure 10b exhibits the corresponding objective functions for precalibration and postcalibration experiments. Precalibration experiments show again high values of the objective function in all seasons, with highest values in DJF, an indication of the errors in the

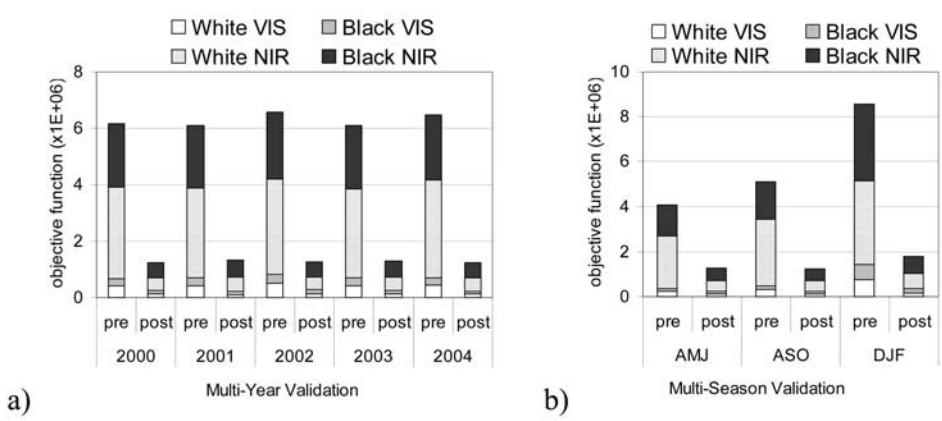

Figure 10. (a) Objective function (Ψ) of spectral surface albedo for precalibration and postcalibration simulations for March, July, November in 2000 (calibrated year), and 2001 $\sim$ 2004 (validation years). (b) Objective function (Ψ) of spectral surface albedo for precalibration and postcalibration simulations for AMJ (April–May–June), ASO (August–September–October), and DJF (December–January–February) in 2000. January and February correspond to 2001.

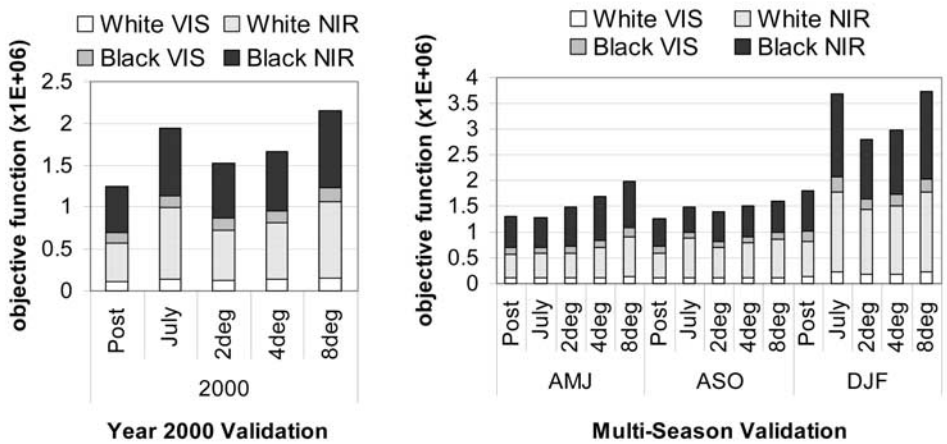

Figure 11. The objective functions of limited-site and limited-time calibrations are compared with continental-scale calibration.

stem and soil optical parameters. The postcalibration experiments show small values of the objective functions, particularly in warm seasons, AMJ and ASO. Similar to the precalibration experiments, the objective function in DJF appears to be larger than those in AMJ and ASO. This study used the spatially continuous snow-free albedo, which interpolate the missing or snow-covered pixel [*Moody et al.*, 2005]. In DJF, the snow cover is often extensive in the northern portion of United States, and the effect on surface albedo was unnaturally removed during the calibration process. However, the soil moisture is usually saturated beneath the snow in ULM, and it increases the discrepancy from the interpolated MODIS albedo in DJF (not shown here).

[45] While the calibrations are conducted in three separate months in 2000, the set of calibrated parameters also improved the representation of albedo in ULM for the noncalibrated period at the same level. This suggests that (1) interannual variability of albedo is lower than seasonal variability [*Wang et al.*, 2004] and (2) multiseason calibration successfully generalize the set of tunable coefficients, while avoiding the overfitting of particular components of the optical parameters.

5.5. Local- and Large-Scale Calibration

[46] This section compares the postcalibrated albedo with those calibrated in the limited-time period as well as for limited grid points. The different methods used for calibrating albedos are compared in terms of the objective function (Ψ). Four additional calibrations were conducted. The first experiment is to calibrate a set of tunable parameters only in July, which represent the limited-time calibration (denoted as *July*). The second, third, and forth experiments use the model grid of only every 2, 4, and 8 degrees in latitude and longitude direction (denoted as *2deg*, *4deg*, and *8deg*, respectively). For example, because this study uses a 0.25° grid, *2deg* experiment uses approximately $(.25/2)^2$ = 1/64 of the total grid points that are in the *post* experiment (= 175,800). Thus the *8deg* experiment uses the least grid points $[(.25°/8°)^2 = 1/1024]$.

[47] These experiments derived four different sets of tunable parameters for the given number of grid points and periods. These derived sets of tunable parameters are tested for the entire domain (every grid point for a total of 175,800 grid points) in a similar manner as in section 5.4. Figure 11 shows the objective functions of the limited-time and limited-site calibrations. The *July* experiment has the higher Ψ (1.93×10^6) than that of the *post* experiment (1.24×10^6) in a March–June–November period of 2000. The *July* experiment shows a nearly identical Ψ in the AMJ period, a slightly higher Ψ in the ASO period, and is twice higher in the DJF period in comparison with that of the *post* experiment. This clearly shows that the limited-time calibration tends to localize a set of tunable parameters for the limited calibration period. The *2deg*, *4deg*, and *8deg* experiments show the trend of Ψ, which are gradually increased from the *2deg* to *8deg* experiments. This suggests that a fewer number of the calibrated grid points tends to localize the tunable parameters for the calibrated points.

[48] Although the localizing tendency is shown, the limited-site calibration even reduces the Ψ significantly from the *post* experiment (Figure 10) and it reduces the wall-clock time of calibration time linearly with respect to the grid number. Thus there could be an optimal grid-volume reduction method for the continental calibration. For example, the EOF technique can be used to derive the grids and periods with the most representative combination of LAI, SAI and top-soil moisture for the large-scale domain. Together with a parallel simulation environment, this could considerably reduce the wall-clock time of the continental-scale calibration process, while the detailed method can be examined for future study.

5.6. Sensitivity of Albedo Calibration to the Surface Heat Flux and Temperature

[49] The sensitivity of the simulated surface energy budget to the albedo calibration was addressed using precalibrated and postcalibrated surface albedo for the June–July–August period in 2000. The initial conditions and meteorological forcings are set identically between the experiments. Figure 12 shows the difference (postcalibration − precalibration) at 18:00 Z (around local noon time) of net shortwave radiation, available energy (sensible heat flux + latent heat

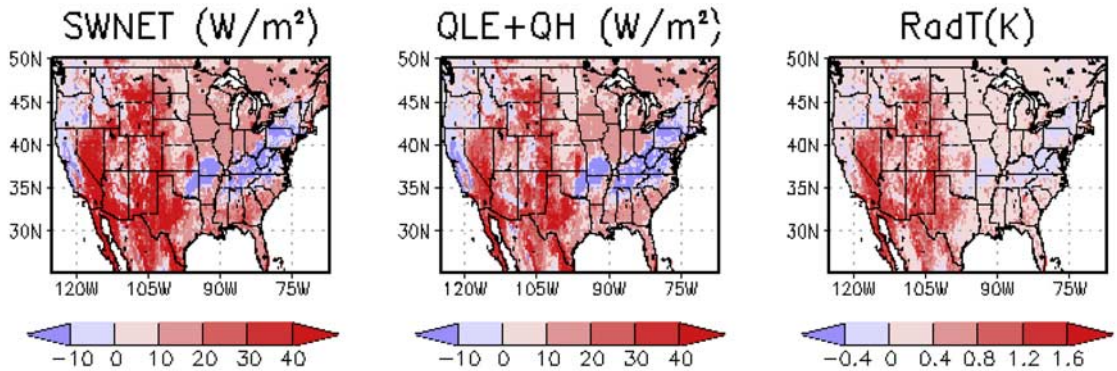

Figure 12. Sensitivity to albedo calibration (POST-EXP − PRE-EXP) of net shortwave radiation (SWNET), available energy (QLE + QH), and radiative temperature (RadT) averaged over June–July–August 2000.

flux), and radiative temperature averaged over the simulated period. Overall, the simulated surface energy budget has been changed significantly over the less-vegetated regions after the calibration. The largest difference exists over southwest United States and Mexico, particularly over Great Basin, Chihuahuan Desert and Baja California. In those regions, net shortwave radiation and available energy increased by more than 40 Wm^{-2} and radiative temperature by more than 1.6 K in the postcalibration experiments. On the other hand, net shortwave radiation, available energy, and radiative temperature were slightly decreased over the Appalachian Mountains, where the dominant LULC class is the broadleaf forest. The postcalibration simulation tends to improve the performance of the model LST in comparison with MODIS LST (also discussed in the follow-up study [*Matsui*, 2006]). However, this improvement simultaneously depends on other parameters related to the function of surface heat flux in the ULM. Thus we should note that the improvement of simulated albedo might not improve overall performance for different LSMs.

6. Summaries and Discussions

[50] We established the continental-scale multiobservation calibration system for Colorado State University (CSU) unified land model (ULM) in the Land Information System (LIS) coupled with the Parameter Estimation (PEST) model. The simulation domain comprised 16,648 land grid points and a total 61,883 subgrid tiles over the conterminous United States (CONUS), which enabled a more robust calibration process than a limited-site calibration does. This paper aimed to calibrate the vegetation and soil optical properties by comparing model- and satellite-derived surface spectral albedos. The four different types of MODIS surface albedo, including black- and white-sky albedo for the visible (VIS) and near-infrared (NIR) bands were compared with the corresponding direct- and diffuse-radiation albedos for the VIS and NIR bands from the two-stream canopy radiative transfer (TCRT) and soil albedo model. Leaf and stem reflectances (ρ_{leaf}^{VIS}, ρ_{leaf}^{NIR}, ρ_{stem}^{VIS}, and ρ_{stem}^{NIR}), the departure of leaf angles from a random distribution (χ_L) for seven bundled LULC classes, in addition to the four parameters (a^{VIS}, b^{VIS}, a^{NIR}, and b^{NIR}) for new soil albedo parameterization were selected and calibrated via the Gauss-Marquardt-Levenberg (GML) algorithm. A new tunable soil albedo parameterization was developed as a function of log-normalized difference L_{max} (*LND*). Three months from 2000, March, July and November, were selected for the calibration, because these characterize the early development, maturity and senescence, respectively, of the vegetation over United States.

[51] Although the ULM initialization used a consistent set of the MODIS LAI and LULC, it was not guaranteed that the ULM would predict surface spectral albedos consistent with those observed from the MODIS radiances. ULM also showed that the experiment with the original set of parameters slightly overestimated the VIS black- and white-sky surface albedo in shrublands and grasslands over the central United States, and strongly overestimated the NIR black- and white-sky albedo in the most of the LULC classes. The strong biases of VIS surface albedo in shrublands and grasslands are probably due to fact that the analytic solution of the original TCRT was derived under an assumption of semi-infinite canopy [*Dickinson*, 1983], which is an inappropriate assumption for less-vegetated LULC classes.

[52] The GML calibration process takes approximately five iterations to achieve the convergence. The entire calibration process reduced the Ψ (a weighted sum of squared deviation between model and observation) by 18.3% of Ψ before the calibration ($\Psi = 6.12 \times 10^6$). After the initial calibration, ULM with a set of tuned optical parameters significantly reduced the biases in the VIS albedo for shrublands and grasslands over the central United States and the biases appeared in NIR albedo for most of the LULC classes. The lowered standard deviations of errors suggest that the new adjustable soil albedo parameterization together with the tuned vegetation optical parameters improved the spatial representation of surface albedo in ULM in comparison with MODIS albedo.

[53] Multiobservation (black- and white-sky albedo) calibration revealed that the upscattering fraction for diffuse radiation was too high and physically unfeasible. Thus we integrated the direct-radiation upscattering fraction of nine sky angles for the diffuse-radiation upscattering fraction, which solved the issue (2) raised after the initial calibration. A second calibration was implemented from the lessons

learned from the first calibration: (1) the functional error in diffuse-radiation upscattering fraction was fixed, (2) manually fixed the surface albedo for the urban class (0.06 for VIS and 0.20 for NIR based on the mean albedo of urban pixel from the MODIS), and (3) χ_L was retained as the initial value (not calibrated). This second calibration show an overall improvement of albedo from the precalibration and initial calibration experiments, while retaining the set of more realistic values of parameters than those from after the initial calibration process.

[54] Although the calibrations were conducted only in March, July and November in 2000, the set of calibrated parameters also improved the representation of albedo in ULM for noncalibrated periods at the same level. This demonstrates the robustness of the albedo calibration period designed in this study. On the other hand, another validation shows that the limited-time and limited-site calibration tends to localize sets of tunable parameters for a given calibrated periods and time. Some may inquire on the justification of tuned leaf/stem optical properties, which deviate from the literature-reviewed values [*Dorman and Sellers*, 1989; *Bonan et al.*, 2002]. This can be explained as follows. Usually optical properties are adjusted according to the simplification of a radiative transfer scheme. For example, atmospheric one-dimensional two-stream radiative transfer modifies the atmospheric optical properties through the delta adjustment in order to account for the forward scattering peak [e.g., *Joseph et al.*, 1976]. Similarly, this calibration process can be judged as the adjustment of leaf/stem optical properties so as to account for the several assumptions in the TCRT, including two-stream intensity, isotropic scattering, single-scattering assumption, plane-parallel canopy, semi-infinite canopy, and linear interpolation between the leaf and stem optical properties [*Dickinson*, 1983; *Sellers*, 1985]. The derived set of optical parameters can be applied to other model as the default values as long as using the same set of the parameterization and the MODIS products.

[55] It is worthwhile to refer to the study described by *Tian et al.* [2004]. They reduced the biases of albedo in CLM2 with given vegetation optical properties by incorporating the new 500m MODIS Vegetation Continuous Fields (VCF) [*Hansen et al.*, 2000] and consistent MODIS BU LAI, and Plant Functional Types LULC maps. However, a note of caution about this approach needs to be mentioned here. BU LAI uses the specific LULC class (bundled UMD type LULC) to derive the 1-km LAI map, while Hansen et al. use their own algorithm to derive the fraction of forests and grasslands in the VCF. As *Myneni et al.* [2002] has shown, LAI biases become large if the LULC category is misclassified between forests and grasslands. Therefore the use of both BU LAI and VCF would be appropriate, only if the BU LAI algorithm consistently uses VCF for the derivation of LAI. The VCF and LANDSAT-level high-resolution LULC sets will be eventually required to correctly classify the LULC and to accurately derive the LAI and surface albedo.

[56] The sensitivity of simulated the surface energy budget to albedo calibration was addressed using precalibration and postcalibrated surface albedos for summer (June–July–August) 2000. The largest difference occurred over southwest United States and Mexico, particularly over Great Basin, Chihuahuan Desert and Baja California. In those regions, net shortwave radiation and available increased by more than 40 Wm^{-2} and radiative temperature by more than 1.6 K in the postcalibrated experiment. This suggests that these biases could have a prominent effect on the regional/global climate simulations.

[57] Thus we conclude the following.

[58] 1. Continental-scale calibration improved the model representation of surface albedo over the entire domain in comparison with the operational MODIS snow-free albedo, although the set of the tuned parameters might not be the global optima.

[59] 2. Continental-scale calibration suggests the functional error in the model. We found the errors in the formulation of diffuse-radiation upscattering fraction in the original TCRT model. The model must be corrected to reduce the overestimation of white-sky albedo. Our suggested formula would be easy to incorporate into different models that use TCRT.

[60] 3. The leaf angle distribution function cannot be calibrated probably because of the fundamental difference between the formulations used in the TCRT model the MODIS operational albedo products.

[61] 4. The albedo in ULM was improved for not only the calibrated period but also noncalibrated years and seasons. The choice of calibration periods must be short for computational efficiency, but needs to have as large a variation in the calibrating parameters as possible for the representativeness of the tuning parameters. This enables an efficient, robust calibration process.

[62] 5. Errors in the surface albedo directly control the surface energy and mass flux in the land surface model (LSM). Because all LSMs use a different set of parameterizations and data sets, albedo calibration over the simulated domain must occur first.

[63] The continental-scale calibration that we propose need to be developed further. There are a variety of data to be incorporated in the optimization processes, and the optimization algorithm should be improved. Once, more detailed error structures in the MODIS and other satellite land products are known, the covariance of observation errors can be utilized in the optimization process. Additional validation studies for the MODIS products should reveal such detailed error structures [*Morisette et al.*, 2002]. Although this study uses the simple local search (GML) algorithm for the optimization process, a population-evolution-based global optimization method could ideally be applied to the continental-scale calibration process. This can be achieved by either using a super computing environment or by reducing the number of land-grid points via empirical orthogonal functions or singular value decomposition techniques. Likely, these updates will be presented and published elsewhere in the near future.

[64] **Acknowledgments.** This work is funded by NASA CEAS fellowship (NAG512105), NASA Radiation (NNG04GB87G), NASA Terrestrial Hydrology (NNG05GQ47G), and NASA Interdisciplinary Sciences (NNG04GL61G). The authors thank Eric Moody for providing the snow-free continuous MODIS surface product, Brian Cosgrove and Kristi Arsenault for providing the NLDAS forcing data set, Jim Geiger and Sujay Kumar for developing/installing NASA Land Information System, Tony Arcieri and Michael Aumock for assisting with parallel computational resources, and two anonymous reviewers for improving the manuscript.

References

Baginska, B., W. Milne-Holme, and P. S. Cornish (2003), Modelling nutrient transport in Currency Creek, NSW, with AnnAGNPS and PEST, *Environ. Modell. Software*, *18*, 801–808.

Baldocchi, D. D., et al. (2001), FLUXNET: A new tool to study the temporal and spatial variability of ecosystem-scale carbon dioxide, water vapor and energy flux densities, *Bull. Am. Meteorol. Soc.*, *82*, 2415–2434.

Bonan, G. B., K. W. Oleson, M. Vertenstein, and S. Levis (2002), The land surface climatology of the Community Land Model coupled to the NCAR Community Climate Model, *J. Clim.*, *15*, 3123–3149.

Chen, D.-X., and M. B. Coughenour (1994), GEMTM: A general model for energy and mass transfer of land surfaces and its application at the FIFE sites, *Agric. For. Meteorol.*, *68*, 145–171.

Cosgrove, B. A., et al. (2003), Real-time and retrospective forcing in the North American Land Data Assimilation System (NLDAS) project, *J. Geophys. Res.*, *108*(D22), 8842, doi:10.1029/2002JD003118.

Dickinson, R. E. (1983), Land surface processes and climate-surface albedos and energy balance, *Adv. Geophys.*, *25*, 305–353.

Dickinson, R. E., P. J. Sellers, and D. S. Kimes (1987), Albedo of homogeneous semi-infinite canopies: Comparison of two-stream analytic and numerical solutions, *J. Geophys. Res.*, *92*, 4282–4286.

Dickinson, R. E., A. Henderson-Sellers, and P. J. Kennedy (1993), Biosphere Atmosphere Transfer Scheme (BATS) Version le as coupled to the NCAR Community Climate Model, *NCAR/TN-387+STR*, 72 pp., Natl. Cent. for Atmos. Res., Boulder, Colo.

Doherty, J. (2004), *PEST Model-Independent Parameter Estimation User Manual*, 5th ed., Watermark Numerical Computing, Corinda, Queensland, Australia. (Available at http://www.sspa.com/pest/pestsoft.html)

Dorman, J. L., and P. J. Sellers (1989), A global climatology of albedo, roughness length and stomatal resistance for atmospheric general circulation models as represented by the Simple Biosphere Model (SiB), *J. Appl. Meteorol.*, *28*, 833–855.

Duan, Q., V. K. Gupta, and S. Sorooshian (1993), Shuffled complex evolution approach for effective and efficient global minimization, *J. Optim. Theor. Appl.*, *76*, 501–521.

Goudriaan, J. (1977), *Crop Micrometeorology: A Simulation Study*, 249 pp., Cent. for Agric. Publ. and Doc., Wageningen, Netherlands.

Gupta, H. V., L. A. Bastidas, S. Sorooshian, W. J. Shuttleworth, and Z. L. Yang (1999), Parameter estimation of a land surface scheme using multicriteria methods, *J. Geophys. Res.*, *104*, 19,491–19,504.

Hansen, M. C., R. S. DeFries, J. R. G. Townshend, and R. Sohlberg (2000), Global land cover classification at 1 km spatial resolution using a classification tree approach, *Int. J. Remote Sens.*, *21*, 1331–1364.

Henderson-Sellers, A., A. J. Pitman, P. Irannejad, and K. McGuffie (2002), Land surface simulations improve atmospheric modeling, *Eos Trans. AGU*, *83*, 145152.

Idso, S. B., R. D. Jackson, R. J. Reginato, B. A. Kimball, and F. S. Nakayama (1975), The dependence of bare soil albedo on soil water content, *J. Appl. Meteorol.*, *14*, 109–113.

Jensen, J. R. (2000), *Remote Sensing of the Environment: An Earth Resource Perspective*, 544 pp., Prentice-Hall, Upper Saddle River, N. J.

Jin, Y., C. B. Schaaf, F. Gai, X. Li, A. Strahler, W. Lucht, and S. Liang (2003), Consistency of MODIS surface BRDF/Albedo retrievals: 2. Validation, *J. Geophys. Res.*, *108*(D5), 4159, doi:10.1029/2002JD002804.

Joseph, J. H., W. J. Wiscombe, and J. A. Weinman (1976), The delta-Eddington approximation for radiative transfer, *J. Atmos. Sci.*, *33*, 2452–2459.

Justice, C. O., J. R. G. Townshend, E. F. Vermote, E. Masuoka, R. E. Wolfe, N. Saleous, D. P. Roy, and J. T. Morisette (2002), An overview of MODIS land data processing and product status, *Remote Sens. Environ.*, *83*, 3–15.

Knyazikhin, Y., J. V. Martonchik, R. B. Myneni, M. Verstraete, B. Pinty, and N. Gobron (1998), Synergistic algorithm for estimating vegetation canopy leaf area index and fraction of absorbed photosynthetically active radiation from MODIS and MISR data, *J. Geophys. Res.*, *103*, 32,257–32,274.

Lee, T. J., R. A. Pielke, and P. W. Mielke Jr. (1995), Modeling the clear-sky surface energy budget during FIFE87, *J. Geophys. Res.*, *100*, 25,585–25,593.

Liu, Y. B., O. Batelaan, F. D. Smedt, J. Poórová, and L. Velcická (2005), Automated calibration applied to a GIS-based flood simulation model using PEST, in *Floods, From Defense to Management*, edited by J. Van Alphen et al., pp. 317–326, Taylor and Francis, Philadelphia, Pa.

Matsui, T. (2006), Aerosol effects on cloud-precipitation and land-surface processes, Ph.D. dissertation, 262 pp., Dep. of Atmos. Sci., Colo. State Univ., Fort Collins.

Matsui, T., V. Lakshmi, and E. E. Small (2005), The effects of satellite-derived vegetation cover variability on simulated land–atmosphere interactions in the NAMS, *J. Clim.*, *18*, 21–40.

Moody, E. G., M. D. King, S. Platnick, C. B. Schaaf, and F. Gao (2005), Spatially complete global spectral surface albedos: Value-added datasets derived from Terra MODIS land products, *IEEE Trans. Geosci. Remote Sens.*, *43*, 144–158.

Morisette, J. T., J. L. Privette, and C. O. Justice (2002), A framework for the validation of MODIS land products, *Remote Sens. Environ.*, *83*, 77–96.

Myneni, R. B., et al. (2002), Global products of vegetation leaf area and fraction absorbed PAR from year one of MODIS data, *Remote Sens. Environ.*, *83*, 214–231.

Norman, J. M., and P. G. Jarvis (1975), Photosynthesis in Sitka spruce: Radiation penetration theory and a test case, *J. Appl. Ecol.*, *12*, 839–878.

Niyogi, D., S. Raman, and K. Alapaty (1999), Uncertainty in specification of surface characteristics, Part 2–Hierarchy of interaction explicit statistical analysis, *Boundary Layer Meteorol.*, *91*, 341–366.

Oleson, K. W., G. B. Bonan, C. Schaaf, F. Gao, Y. Jin, and A. Strahler (2003), Assessment of global climate model land surface albedo using MODIS data, *Geophys. Res. Lett.*, *30*(8), 1443, doi:10.1029/2002GL016749.

Oleson, K. W., et al. (2004), Technical description of the Community Land Model (CLM), *NCAR/TN-461+STR*, Cent. for Atmos. Res., Boulder, Colo.

Peters-Lidard, C. D., S. Kumar, Y. Tian, J. L. Eastman, and P. Houser (2004), Global urban-scale land-atmosphere modeling with the land information system, paper presented at Symposium on Planning, Nowcasting, and Forecasting in the Urban Zone, Am. Meteorol. Soc., Seattle, Wash.

Pielke, R. A., Sr. (2001), Influence of the spatial distribution of vegetation and soils on the prediction of cumulus convective rainfall, *Rev. Geophys.*, *39*, 151–177.

Pitman, A. J. (2003), The evolution of, and revolution in, land surface schemes designed for climate models, *Int. J. Climatol.*, *23*, 479–510.

Pitman, A. J., et al. (1999), Key results and implications from Phase 1 (c) of the Project for Intercomparison of Land-surface Parameterization Schemes, *Clim. Dyn.*, *15*, 673–684.

Reichstein, M., et al. (2003), Modeling temporal and large-scale spatial variability of soil respiration from soil water availability, temperature and vegetation productivity indices, *Global Biogeochem. Cycles*, *17*(4), 1104, doi:10.1029/2003GB002035.

Reynolds, C. A., T. J. Jackson, and W. J. Rawls (1999), Estimating available water content by linking the FAO soil map of the world with global soil profile databases and pedo-transfer functions, *Eos Trans. AGU*, *80*(17), Spring Meet. Suppl., Abstract H41D-12.

Schaaf, C. B., et al. (2002), First operational BRDF, albedo and nadir reflectance products from MODIS, *Remote Sens. Environ.*, *83*, 135–148.

Sellers, P. J. (1985), Canopy reflectance, photosynthesis and transpiration, *J. Remote Sens.*, *6*, 1335–1372.

Sellers, P. J., D. A. Randall, G. J. Collatz, J. A. Berry, C. B. Field, D. A. Dazlich, C. Zhang, G. D. Collelo, and L. Bounoua (1996), A revised land surface parameterization (SiB2) for atmospheric GCMs. Part I: Model formulation, *J. Clim.*, *9*, 676–705.

Tian, Y., R. E. Dickinson, L. Zhou, R. B. Myneni, M. Friedl, C. B. Schaaf, M. Carroll, and F. Gao (2004), Land boundary conditions from MODIS data and consequences for the albedo of a climate model, *Geophys. Res. Lett.*, *31*, L05504, doi:10.1029/2003GL019104.

Vrugt, J. A., H. V. Gupta, L. A. Bastidas, W. Bouten, and S. Sorooshian (2003), Effective and efficient algorithm for multiobjective optimization of hydrologic models, *Water Resour. Res.*, *39*(8), 1214, doi:10.1029/2002WR001746.

Walko, R. L., et al. (2000), Coupled atmosphere-biophysics-hydrology models for environmental modeling, *Appl. Meteorol.*, *39*, 931–944.

Wan, Z., Y. Zhang, Q. Zhang, and Z.-L. Li (2002), Validation of the land-surface temperature products retrieved from Terra Moderate Resolution Imaging Spectroradiometer data, *Remote Sens. Environ.*, *83*, 163–180.

Wang, Y.-P., R. Leuning, H. A. Cleugh, and P. A. Coppin (2001), Parameter estimation in surface exchange models using nonlinear inversion: How many parameters can we estimate and which measurements are most useful?, *Global Change Biol.*, *7*, 495–510.

Wang, Z., X. Zeng, M. Barlage, R. E. Dickinson, F. Gao, and C. B. Schaaf (2004), Using MODIS BRDF and albedo data to evaluate global model land surface albedo, *J. Hydrometeorol.*, *5*, 3–14.

Wood, E. F., et al. (1998), The Project for Intercomparison of Land-surface Parameterization Schemes (PILPS) Phase 2C Red-Arkansas River Basin experiment: 1. Experiment description and summary intercomparison, *Global Planet. Change*, *19*, 115–135.

Xiong, X., K. Chiang, J. Esposito, B. Guenther, and W. Barnes (2003), MODIS on-orbit calibration and characterization, *Metrologia*, *40*, S89–S92, PII:S0026-1394 (03)56883-9.

Xue, Y., P. J. Sellers, J. L. Kinter, and J. Shukla (1991), A simplified biosphere model for global climate studies, *J. Clim.*, *4*, 345–364.

Yang, W. Z., et al. (2006), MODIS leaf area index products: From validation to algorithm improvement, *IEEE Trans. Geosci. Remote Sens.*, *44*, 1885–1898.

Zhou, L., et al. (2003), Comparison of seasonal and spatial variations of albedos from Moderate-Resolution Imaging Spectroradiometer (MODIS) and Common Land Model, *J. Geophys. Res.*, *108*(D15), 4488, doi:10.1029/2002JD003326.

A. Beltrán-Przekurat and R. A. Pielke Sr., Department of Atmospheric and Oceanic Sciences, Cooperative Institute for Research in Environmental Science, University of Colorado, Boulder, CO 80309, USA. (adrian@cires.colordo.edu; pielkesr@cires.colorado.edu)

M. B. Coughenour, Natural Resource and Environmental Laboratory, Colorado State University, Campus Mail 1499, Fort Collins, CO 80523-1499, USA. (mikec@nrel.colostate.edu)

T. Matsui, NASA Goddard Space Flight Center, Code 913.1, Greenbelt, MD 20771, USA. (matsui@agnes.gsfc.nasa.gov)

D. Niyogi, Department of Agronomy and Department of Earth and Atmospheric Sciences, Purdue University, 201 LSPS, 915 West State Street, West Lafayette, IN 47906-2054, USA. (dniyogi@purdue.edu)